

Image-Based Background Phase Error Correction in 4D Flow MRI Revisited

Julia Busch, PhD,¹ Daniel Giese, PhD,² and Sebastian Kozerke, PhD^{1,3*}

Purpose: To correct background phase errors in phase-contrast magnetic resonance imaging (MRI), image-based correction by referencing through stationary tissue is widely used. The aim of the present study was a detailed assessment of background phase errors in 4D Flow MRI and limitations of image-based correction.

Materials and Methods: In a phantom study, 4D Flow MRI data were acquired for typical settings on two clinical 3T MR systems. Background errors were analyzed with respect to their spatial order and minimum requirements regarding the signal-to-noise ratio (SNR) and the amount of stationary tissue for image-based correction were assessed. For in vivo evaluation, data of the aorta were acquired on one 3T MR system in five healthy subjects including subsequent scans on the stationary phantom as reference.

Results: Background errors were found to exhibit spatial variation of first- to third-order. For correction, a minimum SNR of 20 was needed to achieve an error of less than 0.4% of the encoding velocity. The minimum amount of stationary tissue was strongly dependent on the spatial order requiring at least 25%, 60%, and 75% of stationary tissue for first-, second-, and third-order correction. In vivo evaluation showed that with 35–41% of stationary tissue available only first-order correction yielded a significant reduction ($P < 0.01$).

Conclusion: Background phase errors can range from first to third spatial order in 4D Flow MRI requiring correction with appropriate polynomials. At the same time, the limited amount of stationary tissue available in vivo limits image-based background phase correction to first spatial order.

Level of Evidence: 1

Technical Efficacy: Stage 1

J. MAGN. RESON. IMAGING 2017;46:1516–1525.

In phase-contrast magnetic resonance imaging (PC-MRI) the velocity of objects is encoded into the image phase using bipolar gradient pairs.¹ Hence, time-resolved velocity of flow in the heart or greater vessels can be measured over the cardiac cycle and flow parameters such as stroke volume, forward, regurgitant, or shunt flow can be determined.^{2,3}

While in early work only one velocity direction was acquired in a single or multiple slices,^{2–4} encoding of all three velocity directions over a 3D volume^{5–8} has become of increasing interest and use. The temporally resolved volumetric mapping of all three velocity directions, also referred to as 4D Flow MRI, allows for the calculation of hemodynamic parameters such as pulse wave velocity,⁹ turbulent kinetic energy,^{10,11} pressure difference maps,¹² and flow vorticity.¹³ Furthermore, complex flow patterns can be visualized using streamlines, pathlines,^{14,15} or volume tracking.¹⁶ To this end,

4D Flow MRI has been used for various applications covering the heart, valves, and great vessels.^{17–20} Recently, a consensus statement of the Society of Cardiovascular Magnetic Resonance has been published to promote best practice while summarizing advantages and challenges of 4D Flow MRI.²¹

Besides long scan times, one of the reasons hampering the use of 4D Flow MRI in a clinical setting is its accuracy. Gatehouse et al²² estimated a limit of acceptability of 5% error in stroke volume, which translates into an acceptable average velocity error of 0.6 cm/s or 0.4% of an encoding velocity of 150 cm/s. The same study showed that for such an accuracy to be achieved, postprocessing is required on all MR systems.

Background errors in PC-MRI can have several physical causes including concomitant fields, gradient nonlinearity, eddy-current effects, and mechanical field oscillations,

View this article online at wileyonlinelibrary.com. DOI: 10.1002/jmri.25668

Received May 27, 2016, Accepted for publication Jan 26, 2017.

This article includes Supplementary Material available via the Internet at <http://www.interscience.wiley.com/jpages/xxxx-xxxx/suppmat>.

*Address reprint requests to: S.K., Institute for Biomedical Engineering, University of Zurich and ETH Zurich, Gloriastrasse 35, CH - 8092 Zurich, Switzerland.
E-mail: kozerke@biomed.ee.ethz.ch

From the ¹Institute for Biomedical Engineering, University of Zurich and ETH Zurich, Zurich, Switzerland; ²Department of Radiology, University Hospital Cologne, Cologne, Germany; and ³Division of Imaging Science and Biomedical Engineering, King's College London, London, UK

Additional supporting information may be found in the online version of this article.

leading to phase errors of various temporal and spatial orders.

The concomitant fields are derived from Maxwell equations and can hence be calculated analytically and corrected for in postprocessing.^{23,24} Similarly, gradient nonlinearities are known deviations from linear gradients that result in geometric distortions and an incorrect measure of flow direction and velocity. To correct the effect, gradient nonlinearity can be incorporated into a more generalized reconstruction.^{25,26} Eddy currents are caused by rapidly switching gradients, which induce currents in the gradient coil windings and nearby conducting structures. Eddy currents are generally assumed to be of zeroth and first spatial order and are corrected for using hard- or software preemphasis.^{27,28} Mechanical oscillations are known to cause sideband excitations in spectroscopy. It has been shown recently that they also play a role in PC-MRI measurements.²⁹

Despite the various correction mechanisms, background phase errors due to eddy currents and mechanical oscillations remain a critical factor compromising the accuracy of PC-MRI data. To correct the residual errors, several approaches have been presented. By repeating the PC-MRI sequence on a stationary phantom, background error maps can be obtained.³⁰ A second approach employs estimation of the background error by linear regression of the phase in segmented stationary tissue.^{31–33} An alternative option is the use of a dedicated magnetic field monitoring device to measure the phase evolution during the sequence.²⁹

While a stationary phantom correction is straightforward, it leads to an increase in overall exam time, rendering it often unpractical in a clinical routine setting. In addition, the approach is based on the assumption that background phases are temporally stable, which would allow for the acquisition of an exact scan replica at a later timepoint. Recent studies^{34,35}, however, have shown that this assumption may be violated for scans with high gradient duty cycle due to heating of the gradient support.

Referencing in stationary tissue, on the other hand, can be performed on the data itself and does not require any additional scan time nor dedicated hardware.³² Since the background error has to be extracted from the stationary tissue and extrapolated onto nonstationary regions, a model of the spatial distribution of the error is required. Lankhaar et al³³ tested varying polynomial orders on single-slice PC-MRI data with 1D velocity encoding and stated that a linear model performs best. Recent work³⁶ suggests that higher-order polynomials are necessary to accurately correct for background errors in 4D Flow MRI.

It was the aim of the present study to analyze background phase errors occurring in 4D Flow MRI. Their correction using a polynomial image-based correction is explored with respect to the spatial order used, the signal-to-noise ratio (SNR) requirements, and the amount of

available stationary tissue using phantom measurements and in vivo acquisitions.

Materials And Methods

Phantom Experiments

Phantom measurements were performed on a stationary “thorax” phantom with dimensions $300 \times 220 \times 190 \text{ mm}^3$ gelled with TX151 solidifying powder (Oil Center Research International, Lafayette, LA) to avoid unwanted liquid motion during measurements. The phantom was doped with gadolinium to achieve a longitudinal relaxation time (T_1) on the order of 800 msec and mixed with 3g/L of sodium chloride to reduce signal cancellation from standing waves. A protocol in accordance with recommendations described in the 4D Flow MRI consensus statement²¹ was implemented. A 3D volume was encoded with an isotropic spatial resolution of 2 mm and a slice oversampling factor of 1.28. A receiver bandwidth of 70.4 kHz and a flip angle of 7° was used. The minimum possible echo times (TE) and repetition times (TR) were chosen. The four PC-MRI acquisitions were interleaved every TR and encoded using a balanced four-point scheme.³⁷ Data were reconstructed and corrected for concomitant fields as reported previously^{23,24} using the MRecon software package (GyroTools, Zurich, Switzerland). For phantom measurements, 22 slices were encoded covering a field of view (FOV) of $320 \times 280 \times 44 \text{ mm}^3$. Data were acquired with a partial echo factor of 0.75 and an elliptical k -space shutter was applied in both phase-encoding directions. Data acquisition was prospectively triggered with the electrocardiogram (ECG) signal. A simulated ECG signal with a rate of 60 beats/min was used and 2-fold k -space segmentation applied. Thus, the temporal resolution of the data is equal to eight times the repetition time. The number of heart phases was adjusted to cover an entire RR-interval and ranged from 20–29. Since the background phase is dependent on the flow encoding gradients and echo timepoint within the sequence, data were acquired in three geometries with four different encoding velocities. Accordingly, 12 different test scenarios could be analyzed per scanner including a single-oblique sagittal volume rotated around the feet–head (FH) axis by -20° , a nonrotated transverse volume, and a double-oblique transverse volume rotated around the anterior–posterior (AP) axis by 15° and around the right–left (RL) axis by 40° (Fig. 1). The three different geometries were chosen according to an acquisition of 1) the aortic arch (single-oblique sagittal volume), 2) both the aortic and pulmonary vessels including their valves (transverse volume), and 3) the entire heart in four-chamber view orientation (double-oblique transverse volume). Data were acquired with encoding velocities of 50, 100, 200, and 400 cm/s to cover the range of encoding velocities typically used in clinical settings and for multi-venc approaches.^{10,11,31,38} All phantom data were acquired on two different 3T systems (Philips Healthcare, Best, The Netherlands): a 3T Philips Achieva (60 cm bore size, maximum gradient strength 31 mT/m, slew rate 200 mT/m/ms) and a 3T Philips Ingenia (70 cm bore size, maximum gradient strength 22.5 mT/m, slew rate 200 mT/m/ms) system equipped with a 32- and a 28-channel cardiac coil, respectively. A list of the corresponding echo and repetition times can be found in Table 1.

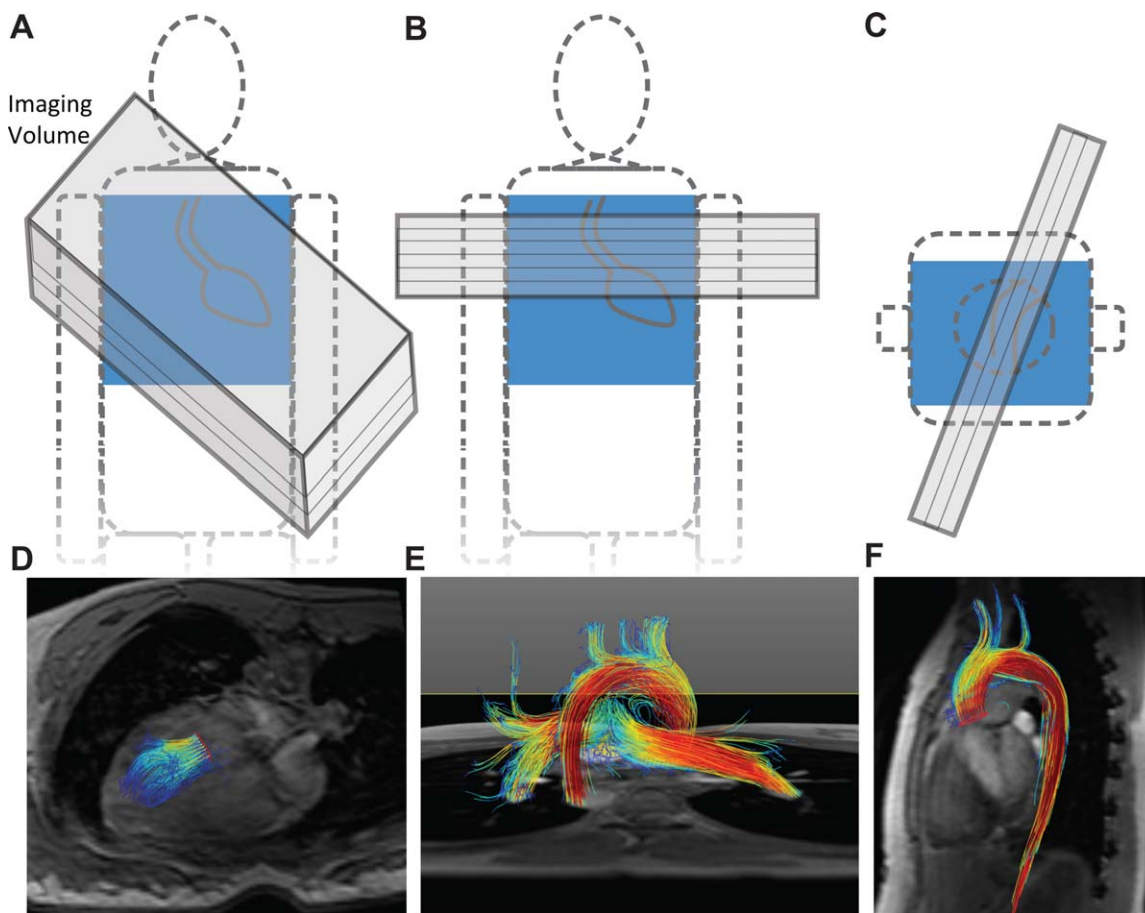


FIGURE 1: Illustration of the three geometries used for acquisition of 4D Flow MRI data along with pathline visualizations of exemplary datasets acquired in vivo; double-oblique transverse volume (A,D), non-rotated transverse volume (B,E), and the single-oblique sagittal volume (C,F).

Data Analysis

All analyses were performed in MATLAB (MathWorks, Natick, MA). The background phase in the stationary phantom data was estimated by linear regression on the 3D volumes using polynomials of zeroth- to sixth-order. Herein, the polynomial order is defined as the highest exponent occurring in the sum. Exemplarily, a second-order polynomial would be defined as:

$$\Phi_{background,2}(x,y,z) \approx a_1x^2 + a_2y^2 + a_3z^2 + a_4xy + a_5xz + a_6yz + a_7x + a_8y + a_9z + a_{10}$$

where a_i are the coefficients of linear regression and x,y,z the spatial coordinates. To assess the quality of linear regression the root-mean-square error (RMSE) was used, defined as:

$$RMSE = \sqrt{\frac{\sum_{i=1}^N (v_i - \tilde{v}_i)^2}{N}}$$

where v_i is the measured data at voxel i , \tilde{v}_i the estimated background phase at voxel i , and N the number of voxels within the object. Throughout this work, the RMSE is stated in percent of the encoding velocity (%venc) and is calculated over the full imaged object volume.

In addition, the mean error over all cubic ROIs of $30 \times 30 \times 30 \text{ mm}^3$ within the volume of the stationary phantom was calculated and the maximum extracted:

$$\max ME_{ROI} = \max_{ROIs} \left(\frac{\left| \sum_{i \in ROI} (v_i - \tilde{v}_i) \right|}{N_{ROI}} \right)$$

The edge length of the ROIs was chosen to be 30 mm in accordance with the diameter of the ascending aorta. For simplicity, the ROI was defined as cubic. The $\max ME_{ROI}$ can directly be translated into the maximum error in stroke volume. Herein, $\max ME_{ROI}$ is stated in %venc and is calculated over the inner 50% of the imaged object volume corresponding to a restricted volume excluding the rim of the phantom in analogy to the stationary tissue in an in vivo case (Fig. 2A). A $\max ME_{ROI}$ of 0.4 %venc is equivalent to 0.6 cm/s for a venc of 150 cm/s.

If not indicated otherwise, the mean and standard deviation of RMSE and $\max ME_{ROI}$ for all geometries are given. The analyses are performed on data from a single (the second) heart phase.

Categorization

After correction of the background phase error, only zero-mean phase noise should remain in the imaging volume and the residual RMSE should correspond to the noise standard deviation of the

TABLE 1. List of All Echo (TE) and Repetition (TR) Times for the Three Geometries and Four Encoding Velocities

		Sagittal, Single-oblique				Transverse				Transverse, Double-oblique			
Venc [cm/s]		50	100	200	400	50	100	200	400	50	100	200	400
60 cm 31/200	TE [msec]	2.6	2.2	1.9	1.8	2.4	2.1	1.9	1.7	2.8	2.3	2.0	1.9
	TR [msec]	4.9	4.5	4.2	4.0	5.6	4.3	4.0	3.9	5.1	4.7	4.3	4.2
70 cm 22.5/200	TE [msec]	2.9	2.4	2.1	1.9	2.7	2.2	2.0	1.8	3.0	2.5	2.2	2.0
	TR [msec]	5.4	4.7	4.5	4.2	5.4	4.5	4.3	4.0	5.6	4.9	4.7	4.3

The scanner type and gradient specifications used are indicated at the left (scanner type; maximum gradient strength [mT/m]/maximum slew rate [mT/m/ms]).

phase images. Assuming a sixth-order polynomial model corrects all systematic phase offsets, the RMSE after correction using a sixth-order polynomial model was assigned as noise standard deviation. To be robust against possible outliers the noise standard deviation σ of the set of experiments was defined as the mean over all RMSEs after correction using a sixth-order polynomial model. The reduction in RMSE ΔRMSE is compared for consecutive polynomial model orders (see Fig. 3). If the relative reduction in RMSE is below a threshold α :

$$\frac{\Delta\text{RMSE}}{\sigma} < \alpha$$

the improvement by increasing the polynomial model by one is rendered negligible. If a sixth-order polynomial model corrects all background phase errors and only noise remains in the image, then the same should hold when performing background phase correction using a seventh-order polynomial model. Accordingly, the relative difference $\frac{|\text{RMSE}_7 - \text{RMSE}_6|}{\sigma}$ after a correction using a seventh-order polynomial model vs. a sixth-order polynomial model denotes the accuracy of the linear regression. On average, $\frac{|\text{RMSE}_7 - \text{RMSE}_6|}{\sigma}$ was measured as 6% with a maximum relative deviation of 21%. Accordingly, the threshold α was set to 30% including some margin. Data were sorted into categories depending on the highest model yielding a substantial improvement. Here, all geometries, encoding velocities and scanner types were considered jointly.

SNR

To assess SNR limitations of image-based background phase correction, complex-valued, zero-mean Gaussian noise of increasing standard deviation was added to the measured k -space data. The velocity-encoded segments were calculated and the noise standard deviation in the phase images was measured after background phase correction using a sixth-order polynomial model in regions of zero mean.

Amount of Stationary Tissue

When acquiring data of the heart or greater vessels, stationary signal is often limited to the anterior (chest) and posterior (back and neck) region. To simulate this effect, linear regression was performed over restricted domains of varying size (Fig. 2B) by

excluding an elliptical area of varying size for the linear regression. Residual error analysis was performed over the entire volume respectively the inner 50% in case of the $\max\text{ME}_{ROI}$.

In Vivo Experiments

All in vivo scans were approved by the local Ethics Committee and informed written consent was obtained from all volunteers prior to measurements.

For identification of typical stationary tissue volumes and locations in vivo, 4D Flow data were acquired in four healthy

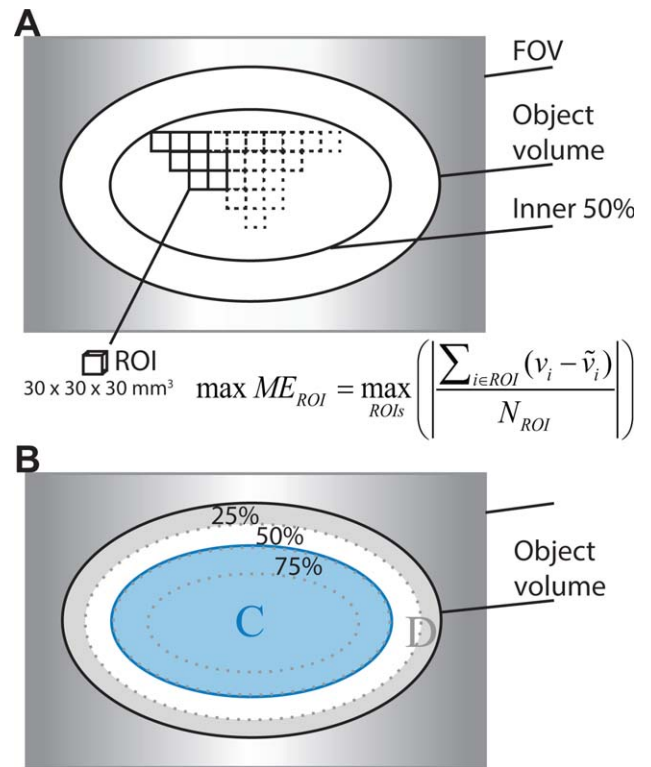


FIGURE 2: Sketch showing the calculation of the $\max\text{ME}_{ROI}$ as the maximum average error over all cubic ROIs of $30 \times 30 \times 30 \text{ mm}^3$ within the inner 50% of the imaged object volume (A). To analyze the effect of limited stationary tissue, background phase errors are estimated based on a limited volume D of varying size while the $\max\text{ME}_{ROI}$ is evaluated on the inner 50% of the imaged object volume C (B).

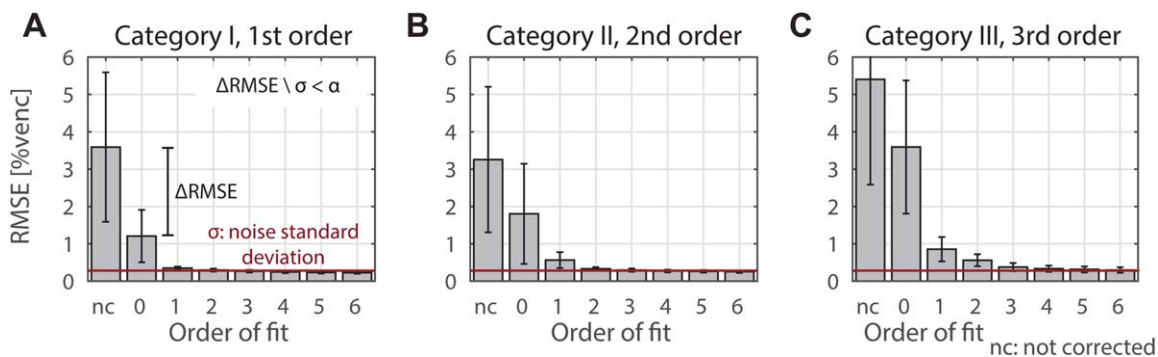


FIGURE 3: RMSE (over the full object volume within the FOV) of the uncorrected data and using polynomials of zeroth- to sixth-order for background phase correction. Data acquired with different geometries and encoding velocities from both the small- and wide-bore system are sorted into three categories depending on the highest polynomial model order yielding a relative improvement in RMSE larger than 30% of the noise level.

volunteers (four female; age: 30 ± 11) with a body mass index ranging from 21–24. Unless indicated otherwise, the same imaging parameters were used as for the phantom acquisitions. Forty-four slices were acquired for the transverse volume covering the aortic arch and the pulmonary arteries as well as for the double-oblique volume covering the whole heart. Additionally, data acquisition was retrospectively triggered with the ECG signal and navigator gating was used to reduce motion artifacts from breathing motion. The encoding velocities were adjusted to the velocity of the blood (ranging from 100–200 cm/s).

For in vivo evaluation, 4D Flow data were acquired in an additional set of five healthy volunteers with a body mass index ranging from 18–23 on the 3T Philips Achieva system (two female, three male; age: 32 ± 10). The acquisition was performed in sagittal orientation covering the ascending aorta and aortic arch using an isotropic encoding velocity of 200 cm/s. The FOV ranged from $320 \times 272 \times 44 \text{ mm}^3$ to $320 \times 304 \times 56 \text{ mm}^3$ with a repetition time of 4.1 msec and an echo time of 1.9 msec. Each in vivo scan was followed by a reference scan on the stationary phantom. To ensure similar thermal conditions of the gradient mount between in vivo and phantom reference scans, a 30-minute gap was included between scans to allow for the gradient mount to cool down to room temperature. Furthermore, k -space data were acquired concentrically starting in the k -space center. For the phantom reference scan a simulated navigator with 50% gating efficiency was applied.

Stationary tissue was determined based on the variance of the image phase over time,³² ie, the squared variance of the phase images over time was segmented using a manually determined threshold of a part per million of the average squared phase variance.

The background phase error maps estimated on the in vivo data using polynomials of zeroth- to third-order were used to correct the in vivo data. Fitting of polynomials higher than third-order was not performed given the limited amount of stationary tissue in vivo. As a reference, the in vivo data were also corrected using the background phase error estimated using a third-order polynomial model on the phantom data. Results were compared using particle tracking through the aortic arch in GTFlow (GyroTools LLC, Zurich, Switzerland). To assess correction results using different polynomial model orders a Welch two-sample t -test was

performed using RStudio (R Core Team, R Foundation for Statistical Computing, Vienna, Austria).

Results

Phantom Experiments

Sorting all phantom datasets into categories depending on the highest polynomial model order required to correct for the background phase error resulted in three categories (Fig. 3). The data acquired on the wide-bore system could be corrected using a first- or second-order polynomial model depending on scan geometry (categories 1 and 2; Fig. 3A,B), whereas the data acquired on the standard-bore system required second- or third-order polynomials to correct for background phase errors (categories 2 and 3; Fig. 3B,C), depending on scan geometry.

In the first category, the RMSE after correction with a first-order polynomial model ranged between 0.31 ± 0.03 %venc and 0.41 %venc (Fig. 4A). For vences 50, 100, 200, and 400 cm/s the $\max ME_{ROI}$ was below 0.4 %venc, which corresponds to 0.6 cm/s for an encoding velocity of 150 cm/s. In the second category (Fig. 4B), the RMSE after correction with a second-order polynomial model was 0.34 ± 0.03 %venc, 0.33 ± 0.03 %venc, 0.33 ± 0.06 %venc and 0.32 ± 0.06 %venc for vences 50, 100, 200, and 400 cm/s, respectively. The $\max ME_{ROI}$ was below 0.4 %venc with values of 0.23 ± 0.04 %venc, 0.24 ± 0.06 %venc, 0.23 ± 0.11 %venc, and 0.24 ± 0.11 %venc for vences 50, 100, 200, and 400 cm/s, respectively. And in the third category (Fig. 4C), the RMSE after correction with a third-order polynomial model was 0.38 ± 0.02 %venc (venc 50 cm/s), 0.41 ± 0.16 %venc (venc 100 cm/s), 0.38 ± 0.09 %venc (venc 200 cm/s), and 0.31 ± 0.07 %venc (venc 400 cm/s) with $\max ME_{ROI}$ values of 0.25 ± 0.07 %venc, 0.23 ± 0.08 %venc, 0.22 ± 0.08 %venc, and 0.20 ± 0.06 %venc.

When decreasing the SNR from 60 to 10, the $\max ME_{ROI}$ increased by 12–43% (Fig. 5) independent of category and encoding velocity with the major increase occurring for SNR smaller 20. At SNR 21 the $\max ME_{ROI}$

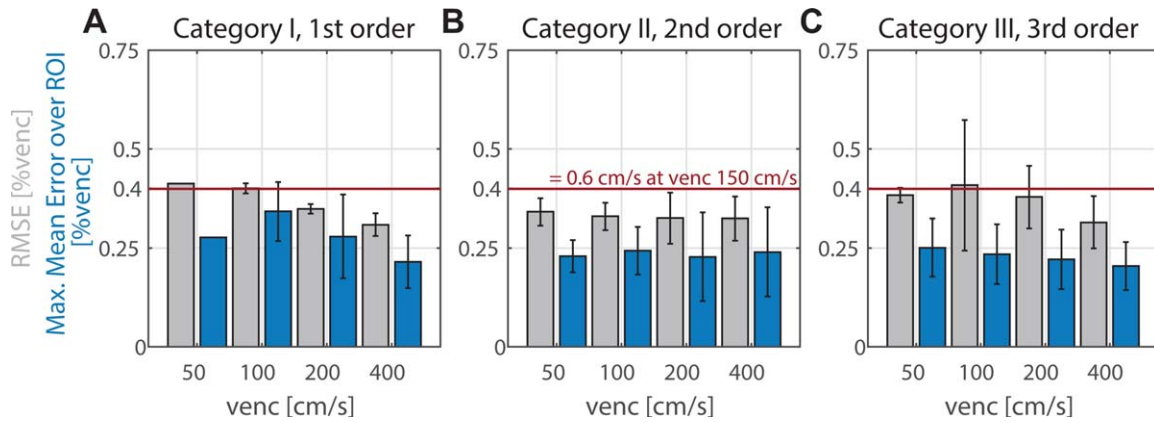


FIGURE 4: Within the three categories the fit residual (RMSE, gray bars) differs only slightly for and not correlated to the different encoding velocities. If the residual consists of Gaussian noise only the RMSE denotes the noise variance of the phase image in %venc. With an exception for category 1 venc 100 cm/s, the $maxME_{ROI}$ is below 0.4 %venc.

was below 0.4 %venc for all datasets except for the group in category 1, with an encoding velocity of 100 cm/s, which showed an already elevated baseline and the group in category 1 with an encoding velocity of 200 cm/s with a $maxME_{ROI}$ of 0.31 ± 0.10 %venc. Despite the seemingly large increase at low SNR, in most cases the $maxME_{ROI}$ was still below 0.4 %venc even at SNR 11. The $maxME_{ROI}$ slightly exceeded 0.4 %venc with 0.38 ± 0.05 %venc in category 1, venc 100 cm/s, 0.33 ± 0.10 %venc in category 1, venc 200 cm/s, 0.31 ± 0.11 %venc in category 2, venc 200 cm/s, and 0.33 ± 0.07 %venc in category 3, venc 50 cm/s.

The volume available for linear regression (stationary tissue) was reduced in eight steps from 100% to 12%. In case of a first-order polynomial background phase correction (Fig. 6A) the reduction in volume available for linear regression from 100% to 12% resulted in an increase in $maxME_{ROI}$ by about 50%. The minimum stationary tissue required to yield an average $maxME_{ROI}$ below 0.4 %venc was 25%. The data acquired with venc 100 cm/s form an exception, with an $maxME_{ROI}$ of 0.40 ± 0.13 %venc at 50% stationary tissue which was caused by the already increased baseline at 100% stationary tissue. For a second-order polynomial background phase correction (Fig. 6B), the $maxME_{ROI}$ at 12% stationary tissue was ~ 3.5 -times larger than when the linear regression was performed over the full imaged object volume. The minimum stationary tissue required to yield an average $maxME_{ROI}$ below 0.4 %venc was 61%. For category 3 (Fig. 6C), the reduction in volume available for linear regression from 100% to 12% yielded a 5–6-fold increase in $maxME_{ROI}$. The minimum stationary tissue required to yield an average $maxME_{ROI}$ below 0.4 %venc was 75%.

In Vivo Experiments

Figure 7 shows exemplary data acquired in healthy volunteers. The stationary tissue used for regression is indicated by the light blue boundary. In the volunteers measured, the

amount of stationary tissue ranged from 37–63% of the total object volume depending on the geometry with an SNR ranging from 20–50.

In the in vivo evaluation, the percentage of stationary tissue ranged from 35–41%. Figure 8A shows the RMSE after background phase correction using zeroth- to third-order polynomial models estimated on the stationary tissue and the full phantom reference for the three flow-encoding directions along the measurement, phase-encode, and slice-select directions. For the phantom reference scan (blue), the RMSE reduced to 1.50 ± 0.62 %venc, 0.61 ± 0.11 %venc, 0.54 ± 0.11 %venc, and 0.48 ± 0.08 %venc using zeroth- to third-order polynomial models. For background phase estimation on the in vivo data (gray), the first-order polynomial correction yielded the smallest residuum with 0.80 ± 0.15 %venc. Particle tracking on in vivo data of the aortic arch corrected using a third-order polynomial model estimate of the phantom reference resulted in $91 \pm 1\%$, $63 \pm 15\%$, and $38 \pm 13\%$ of particles arriving in aortic cross-sections 2, 3, and 4, respectively (Fig. 8B). When comparing particle tracking results of data corrected using polynomial model estimates of zeroth- to third-order with the limited amount of stationary tissue in vivo, a background correction using a first-order polynomial model performed best with $88 \pm 3\%$, $54 \pm 10\%$, and $34 \pm 9\%$ of particles arriving at cross-sections 2, 3, and 4, respectively, and P -values smaller 0.01 when compared to zeroth-order corrections. Yet the background phase error map calculated on the phantom reference outperformed the background estimate using a first-order polynomial model in vivo.

Discussion

In this study, background phase errors of typical 4D Flow MRI data were analyzed regarding their spatial order as a function of scan parameters and gradient configuration, the amount of stationary tissue, and the minimum signal-to-noise ratio required for correction. The results revealed that

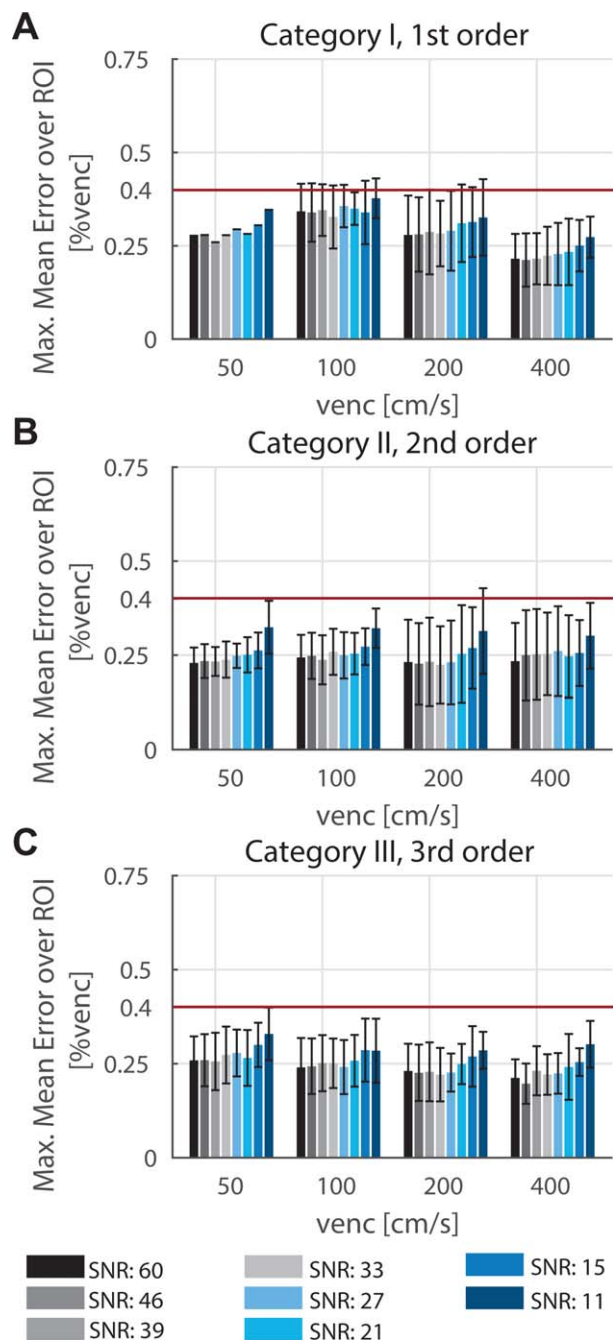


FIGURE 5: The mean $\max ME_{ROI}$ after correction with polynomials of first (A), second (B), and third (C) order are displayed for various SNR levels.

background phase errors can range up to third spatial order requiring correction with appropriate polynomials to yield residual velocity offsets smaller than the acceptable 0.6 cm/s. At the same time, the limited amount of stationary tissue typically available in vivo, however, limits image-based background phase correction to first spatial order in most practical settings.

In a range from 20–60, SNR was found to have little influence on the accuracy of background phase correction with polynomial models of first-, second-, and third-order. For SNR smaller than 20, residual velocity offsets after

background phase correction increased, but typically remained under or only slightly exceeded the limit of 0.6 cm/s. At this point it is important to note that the $\max ME_{ROI}$ indicates the maximum average error over all cubic ROIs of $30 \times 30 \times 30 \text{ mm}^3$ within the inner 50% of the imaged object volume, and thus indicates an upper limit of the residual velocity errors. In general, the residual velocity error increases with increasing distance from the iso-center. Accordingly and depending on the vessel of interest and

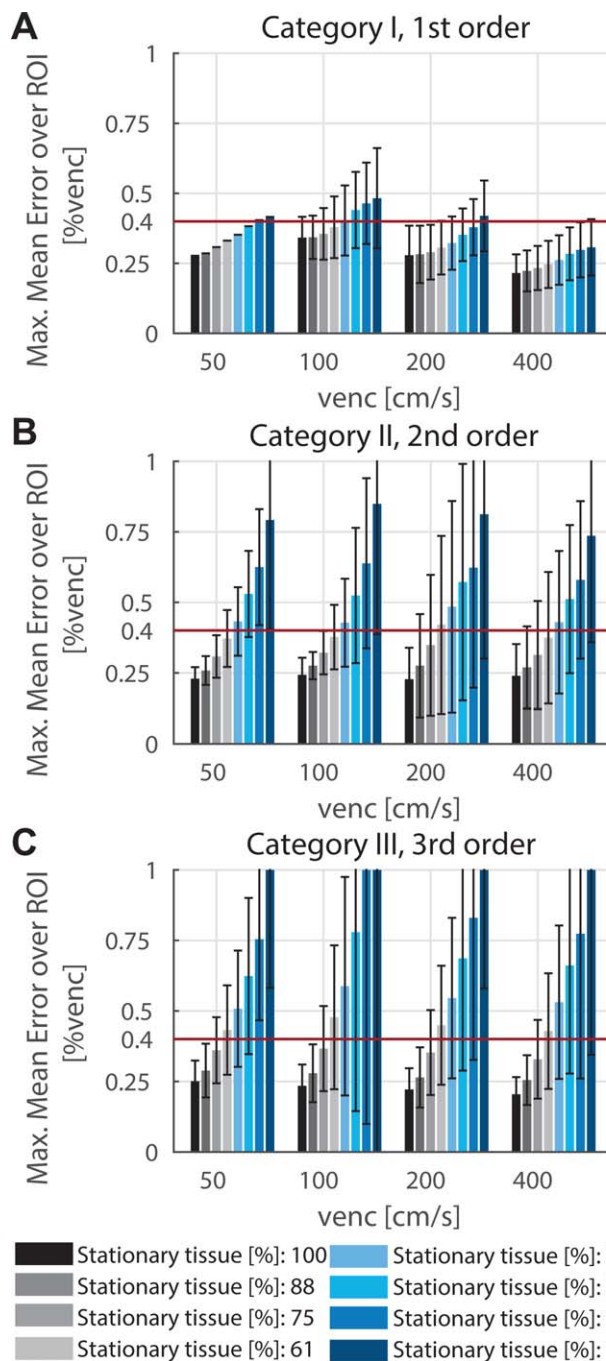


FIGURE 6: Presentation of the mean $\max ME_{ROI}$ after correction with polynomials of first (A), second (B), and third (C) order as a function of the amount of tissue used for the regression.

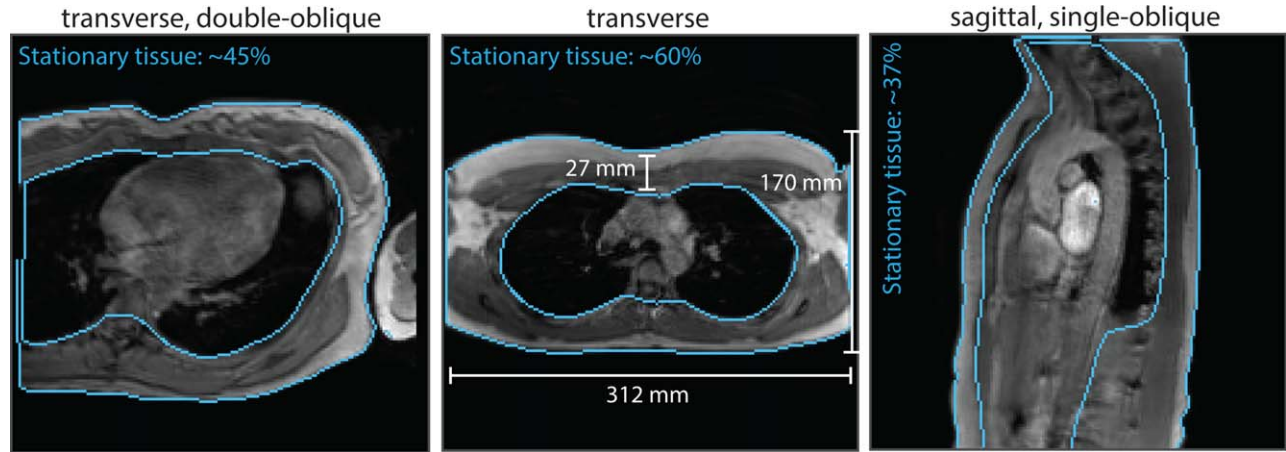


FIGURE 7: Exemplary MRI data acquired in a double-oblique transverse, transverse, and single-oblique sagittal view. The edges of the stationary tissue used for correction of the background phase error by linear regression are indicated in light blue and the amount of stationary tissue is stated.

planning of the FOV in vivo, residual velocity errors may be smaller than the limits reported here.

The limited amount of stationary tissue only has minor effects on first-order polynomial background phase correction, yielding residual velocity offsets below 0.6 cm/s down to a minimum of 25% of stationary tissue. On the other hand, for background phase correction using second- or third-order polynomial models the residual velocity errors rapidly increase, limiting its usability to cases where the amount of stationary tissue exceeds 60 and 75%, respectively. Herein, an elliptical area was cut from the center of the phantom, yielding a rather even distribution of the stationary tissue along the rim of the phantom per slice, as would be achieved by aligning the center of the imaging planes

with the center of the imaged subject. If, however, the FOV was shifted so that there is no stationary tissue on one or more sides, the results presented may not be valid.

If the SNR of the data is very low, averaging several heart phases is a suitable approach to increase SNR of stationary tissue. To this end, continuous acquisition in combination with retrospective cardiac triggering needs to be used.^{6,7} The use of respiratory navigators or other gating strategies can cause an interruption of the eddy-current steady-state, and hence changes in background phase errors over the first heart phases occur.²⁹ Additionally, due to the coarse temporal resolution of the navigator acquisition for respiratory gating, motion artifacts in the later heart phases cannot be fully avoided, as demonstrated in the

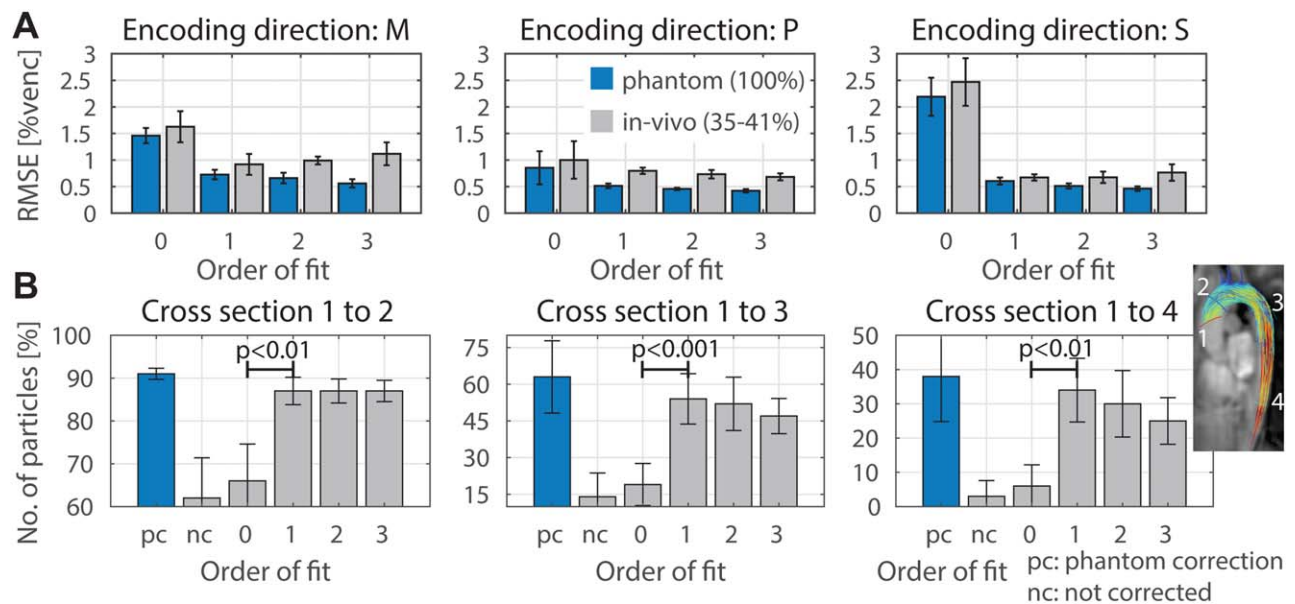


FIGURE 8: In vivo evaluation. Comparison of the RMSE using zeroth- to third-order polynomial models for background phase correction on the full phantom reference scan versus on the limited amount of stationary tissue in vivo (A). Particle tracking results are presented in three cross-sections for in vivo data corrected using background phase estimates in the phantom reference and zeroth- to third-order polynomial models in vivo (B).

Supplemental Material. Remaining breathing motion can cause motion artifacts which can hamper the accuracy of the linear regression causing an increase in the residual error beyond 0.6 cm/s (Supplemental Fig. 1). To avoid false estimation of the background phase error due to motion artifacts, it is hence suggested to correct diastolic heart phases using the background phase estimation performed on systolic heart phases (while excluding the first heart phases after a leading navigator). For example, with a heart phase interval of 50 msec and a heart rate of 60 beats per minute, heart phases between 150–400 msec could be averaged to obtain phase correction maps. Alternatively, data could be acquired without a navigator and motion correction be achieved by retrospective data binning.³⁹

The in vivo evaluation in the aorta has demonstrated that with ~35–40% of stationary tissue available for this scan geometry, only first-order correction yields a significant reduction in background phase error, as exemplified by increased particle trace counts. Nonetheless, first-order correction using stationary tissue from the same scan results in increased errors and reduced particle tracking results when compared to the phantom correction using a third-order polynomial model for estimation of the background offsets. This finding is in line with the original phantom study, which showed that at least 60% and 75% of stationary tissue is required to conduct background phase correction of second and third spatial order, respectively.

In case the amount of stationary tissue is below 30%, a different background phase correction approach such as the acquisition of a separate phantom scan or magnetic field monitoring should be considered. Additionally, the vessel of interest should be placed in the iso-center to avoid contamination with large background phase errors.

Analysis of second- and third-order concomitant fields have shown that the residual higher-order background phase errors cannot be attributed to concomitant fields and thus are attributed to higher-order eddy-currents (data not shown).

The analyses presented here are based on systems from the same vendor. Similar to zeroth- and first-order eddy-currents,^{29,35} higher-order phase errors also exhibit temporal variations over the readout. As a result, a simple change in echo time can cause remarkable changes not only in the amount of background phase error but also in its spatial distribution and order. Hence, acquiring 4D Flow data with different geometries also yields background phase errors of different spatial order. This allowed sorting of all phantom datasets into the three categories to perform more generic analyses on dependency of fitting accuracy and precision on SNR and on the amount of stationary tissue used for linear regression of different polynomial model orders. While this study yielded valuable insights, a general conclusion valid for all available MR systems cannot be drawn. Of note, at

this point in time 4D Flow MRI sequences in accordance with the consensus statement have not been implemented by all vendors,²¹ and hence the present study was restricted to the vendor offering a 4D Flow MRI sequence as a product. To gain a more general conclusion, a multivendor study needs to be performed in the future. However, the dependency of fitting accuracy and precision on SNR and on the amount of stationary tissue used for linear regression are generic.

In conclusion, background phase errors can range from first up to third spatial order, requiring correction with appropriate polynomial orders depending on MR gradient configurations and scan geometry. At the same time, however, the limited amount of stationary tissue typically available in vivo limits image-based background phase error correction to zeroth and first spatial order despite the presence of higher-order background phase errors. It is, however, important to keep in mind that higher-order background errors may occur on some systems and hence restrict the accuracy which can be achieved by image-based background phase correction. To this end, alternative methods including advanced magnetic field monitoring may need to be studied further.

Acknowledgment

Contract grant sponsor: Swiss National Science Foundation; contract grant number: 320030_149567

The authors thank Martin Bührer for support with the MRRecon software package.

References

1. Pelc NJ, Herfkens RJ, Shimakawa A, Enzmann DR. Phase contrast cine magnetic resonance imaging. *Magn Reson Q* 1991;7:229–254.
2. Gatehouse PD, Keegan J, Crowe LA, et al. Applications of phase-contrast flow and velocity imaging in cardiovascular MRI. *Eur Radiol* 2005;15:2172–2184.
3. Kilner PJ, Gatehouse PD, Firmin DN. Flow measurement by magnetic resonance: a unique asset worth optimising. *J Cardiovasc Magn Reson* 2007;9:723–728.
4. Lotz J, Meier C, Leppert A, Galanski M. Cardiovascular flow measurement with phase-contrast MR imaging: Basic facts and implementation. *Radiographics* 2002;22:651–671.
5. Firmin DN, Gatehouse PD, Konrad JP, Yang GZ, Kilner PJ, Longmore DB. Rapid 7-dimensional imaging of pulsatile flow. *Comp Cardiol* 1993;353:2–5.
6. Wigström L, Sjöqvist L, Wranne B. Temporally resolved 3D phase-contrast imaging. *Magn Reson Med* 1996;36:800–803.
7. Markl M, Chan FP, Alley MT, et al. Time-resolved three-dimensional phase-contrast MRI. *J Magn Reson Imaging* 2003;17:499–506.
8. Markl M, Frydrychowicz A, Kozerke S, Hope M, Wieben O. 4D flow MRI. *J Magn Reson Imaging* 2012;36:1015–1036.
9. Mohiaddin R, Firmin D, Longmore D. Age-related changes of human aortic flow wave velocity measured noninvasively by magnetic resonance imaging. *J Appl Physiol* 1993;74:492–497.

10. Dyverfeldt P, Sigfridsson A, Kvitting J-PE, Ebberts T. Quantification of intravoxel velocity standard deviation and turbulence intensity by generalizing phase-contrast MRI. *Magn Reson Med* 2006;56:850–858.
11. Binter C, Knobloch V, Manka R, Sigfridsson A, Kozerke S. Bayesian multipoint velocity encoding for concurrent flow and turbulence mapping. *Magn Reson Med* 2013;69:1337–1345.
12. Ebberts T, Wigström L, Bolger AF, Engvall J, Karlsson M. Estimation of relative cardiovascular pressures using time-resolved three-dimensional phase contrast MRI. *Magn Reson Med* 2001;45:872–879.
13. Von Spiczak J, Crelier G, Giese D, Kozerke S, Maintz D. Quantitative analysis of vortical blood flow in the thoracic aorta using 4D phase contrast MRI. *PLoS One* 2015;10:1–19.
14. Napel S, Lee D, Frayne R, Rutt B. Visualizing three-dimensional flow with simulated streamlines and three-dimensional phase-contrast MR imaging. *J Magn Reson Imaging* 1992;2:143–153.
15. Buonocore MH. Visualizing blood flow patterns using streamlines, arrows, and particle paths. *Magn Reson Med* 1998;40:210–226.
16. Töger J, Carlsson M, Söderlind G, Arheden H, Heiberg E. Volume tracking: a new method for quantitative assessment and visualization of intracardiac blood flow from three-dimensional, time-resolved, three-component magnetic resonance velocity mapping. *BMC Med Imaging* 2011;11:10.
17. Sørensen TS, Beerbaum P, Körperich H, Pedersen EM. Three-dimensional, isotropic MRI: a unified approach to quantification and visualization in congenital heart disease. *Int J Cardiovasc Imaging* 2005;21:283–292.
18. Srichai MB, Lim RP, Wong S, Lee VS. Cardiovascular applications of phase-contrast MRI. *Am J Roentgenol* 2009;192:662–675.
19. Hope MD, Meadows AK, Hope TA, et al. Clinical evaluation of aortic coarctation with 4D flow MR imaging. *J Magn Reson Imaging* 2010;31:711–718.
20. Valverde I, Nordmeyer S, Uribe S, et al. Systemic-to-pulmonary collateral flow in patients with palliated univentricular heart physiology: measurement using cardiovascular magnetic resonance 4D velocity acquisition. *J Cardiovasc Magn Reson* 2012;14:25.
21. Dyverfeldt P, Bissell M, Barker AJ, et al. 4D flow cardiovascular magnetic resonance consensus statement. *J Cardiovasc Magn Reson* 2015;17:72.
22. Gatehouse PD, Rolf MP, Graves MJ, et al. Flow measurement by cardiovascular magnetic resonance: a multi-centre multi-vendor study of background phase offset errors that can compromise the accuracy of derived regurgitant or shunt flow measurements. *J Cardiovasc Magn Reson* 2010;12:5.
23. Norris DG, Hutchison JM. Concomitant magnetic field gradients and their effects on imaging at low magnetic field strengths. *Magn Reson Imaging* 1990;8:33–37.
24. Bernstein MA, Zhou XJ, Polzin JA, et al. Concomitant gradient terms in phase contrast MR: analysis and correction. *Magn Reson Med* 1998;39:300–308.
25. Markl M, Bammer R, Alley MT, et al. Generalized reconstruction of phase contrast MRI: analysis and correction of the effect of gradient field distortions. *Magn Reson Med* 2003;50:791–801.
26. Peeters JM, Bos C, Bakker CJG. Analysis and correction of gradient nonlinearity and B0 inhomogeneity related scaling errors in two-dimensional phase contrast flow measurements. *Magn Reson Med* 2005;53:126–133.
27. Jehenson P, Westphal M, Schuff N. Analytical method for the compensation of eddy-current effects induced by pulsed magnetic field gradients in NMR systems. *J Magn Reson* 1990;90:264–278.
28. Van Vaals J, Bergman A. Optimization of eddy-current compensation. *J Magn Reson* 1990;70:52–70.
29. Giese D, Haeberlin M, Barmet C, Pruessmann KP, Schaeffter T, Kozerke S. Analysis and correction of background velocity offsets in phase-contrast flow measurements using magnetic field monitoring. *Magn Reson Med* 2012;67:1294–1302.
30. Chernobelsky A, Shubayev O, Comeau C, Wolff S. Baseline correction of phase contrast images improves quantification of blood flow in the great vessels. *J Cardiovasc Magn Reson* 2007;9:681–685.
31. Caprihan A, Altobelli S, Benitez-Read E. Flow-velocity imaging from linear regression of phase images with techniques for reducing eddy-current effects. *J Magn Reson* 1990;90:71–89.
32. Walker PG, Cranney GB, Scheidegger MB, Waseleski G, Pohost GM, Yoganathan AP. Semiautomated method for noise reduction and background phase error correction in MR phase velocity data. *J Magn Reson Imaging* 1993;3:521–530.
33. Lankhaar J-W, Hofman MBM, Marcus JT, Zwanenburg JJM, Faes TJC, Vonk-Noordegraaf A. Correction of phase offset errors in main pulmonary artery flow quantification. *J Magn Reson Imaging* 2005;22:73–79.
34. Gatehouse PD, Rolf MP, Bloch KM, et al. A multi-center inter-manufacturer study of the temporal stability of phase-contrast velocity mapping background offset errors. *J Cardiovasc Magn Reson* 2012;14:72.
35. Busch J, Vannesjo SJ, Barmet C, Pruessmann KP, Kozerke S. Analysis of temperature dependence of background phase errors in phase-contrast cardiovascular magnetic resonance. *J Cardiovasc Magn Reson* 2014;16.
36. Ebberts T, Haraldsson H, Dyverfeldt P. Higher order weighted least-squares phase offset correction for improved accuracy in phase-contrast MRI. In: *Proc 16th Annual Meeting ISMRM, Toronto; 2008*. p 1367.
37. Pelc NJ, Bernstein MA, Shimakawa A, Glover GH. Encoding strategies for three-direction phase-contrast MR imaging of flow. *J Magn Reson Imaging* 1991;1:405–413.
38. Lee AT, Pike GB, Pelc NJ. Three-point phase-contrast velocity measurements with increased velocity-to-noise ratio. *Magn Reson Med* 1995;33:122–126.
39. Feng L, Axel L, Chandarana H, Block KT, Sodickson DK, Otazo R. XD-GRASP: Golden-angle radial MRI with reconstruction of extra motion-state dimensions using compressed sensing. *Magn Reson Med* 2016;75:775–788.